Detection and variability of combustion-derived vapor in an urban basin

Richard P. Fiorella[1], Ryan Bares[2], John C. Lin[2], James R. Ehleringer[3], and Gabriel J. Bowen[1]

[1]Department of Geology and Geophysics, University of Utah, 115 S 1460 E, Salt Lake City, UT, 84112, USA
[2]Department of Atmopsheric Sciences, University of Utah
[3]Department of Biology, University of Utah

Correspondence to: Richard Fiorella (rich.fiorella@utah.edu)

Abstract. Water emitted during combustion may comprise a significant portion of ambient humidity (>10%) in urban areas, where combustion emissions are strongly focused in space and time. Stable water vapor isotopes can be used to apportion measured humidity values between atmospherically transported and combustion-derived water vapor, as combustion vapor possesses an unusually negative deuterium excess value (d-excess, $d = \delta^2 H - 8\delta^{18}O$). We investigated the relationship be-
5   tween d-excess of atmospheric vapor, ambient CO_2 concentrations, and atmospheric stability across four winters in Salt Lake City, UT. We found a robust inverse relationship between CO_2 excess above background and d-excess on sub-diurnal to seasonal timescales, which was most prominent during periods of strong atmospheric stability that occur during Salt Lake City winter. We developed a framework for partitioning changes in water vapor d-excess between advective changes in vapor and the addition of combustion derived vapor. Using a Keeling-style mixing model approach, we estimated the d-excess of combustion
10   derived vapor in Salt Lake City to be between $-125‰$ and $-308‰$ broadly consistent with theoretical estimates. Moreover, our analysis highlights that changes in the observed d-excess during periods of high atmospheric stability cannot be explained without a vapor source possessing a strongly negative d-excess value. Further refinements in our estimate of the isotopic composition of combustion derived vapor require constraints on valley-scale stoichiometry between CO_2 and H_2O in combustion products, yet our results demonstrate the utility of stable water vapor isotopes to constrain contributions of combustion to urban
15   humidity and meteorology.

1 Introduction

Fossil fuel combustion releases $\sim 10\,\mathrm{Pg\,y^{-1}}$ of water vapor to the atmosphere. This water flux is negligible in the hydrologic cycle on global and annual timescales (e.g., Trenberth et al., 2006), but it may be significant to urban hydrologic cycling and meteorology as fossil fuel emissions are tightly concentrated in space and time (Bergeron and Strachan, 2012; Duren and
20   Miller, 2012; Gorski et al., 2015; Sailor, 2011; Salmon et al., 2017). In turn, water vapor from fossil fuel combustion may have subsequent impacts on urban air quality and meteorology. However, it remains difficult to partition humidity from combustion-derived vapor (CDV) from "naturally-occurring" or advected water vapor using standard meteorological measurements, making its impact on the urban atmosphere difficult to assess.

Stable water vapor isotopes represent a promising method to apportion observed water vapor between combustion and advection sources (Gorski et al., 2015). Combustion of hydrocarbons produces water from the reaction of atmospheric oxygen, which is ^{18}O-enriched relative to VSMOW (+23.9 ‰, Barkan and Luz, 2005), and structurally-bound fuel hydrogen, which is ^{2}H-depleted relative to VSMOW due to preference for ^{1}H over ^{2}H during biosynthetic reactions (e.g., Estep and Hoering,

5   1980; Sessions et al., 1999). The reaction of ^{18}O-enriched oxygen with ^{2}H-depleted fuels imparts an unusually negative deuterium excess value ($d = \delta^{2}H - 8\delta^{18}O$ Dansgaard, 1964) to product vapor that is distinct in the "natural" hydrological cycle. Deuterium excess is ~ 10 ‰ on average in precipitation (Dansgaard, 1964; Rozanski et al., 1993), and ranges in "natural" waters from +150-200 ‰ in vapor in the upper troposphere (Blossey et al., 2010; Bony et al., 2008; Webster and Heymsfield, 2003) to ~ -60‰ in highly evaporated surface waters (e.g., Fiorella et al., 2015). In contrast, Gorski et al. (2015) estimated

10 CDV d-excess values for fuels in Salt Lake Valley (SLV) ranging from -180 to -470 ‰, depending on the isotopic composition of the fuel and the degree of equilibration of oxygen isotopes between CO_2 and H_2O in combustion emissions.

The SLV forms a basin, within which the Salt Lake City, UT metro area (population of ~ 1.15 million) is located. The SLV is bounded on the west by the Oquirrh Mountains ($\sim 2200 - 2500$ m), on the east by the Wasatch Mountains (>3000 m), and on the south by the Traverse Mountains (< 2000 m). The northwest corner of the basin is bounded by the Great Salt

15 Lake. During the winter, cold air often pools in the SLV, increasing atmospheric stability and limiting transport of combustion products away fromt the city and impairing air quality. Previous work in the SLV indicated that CDV comprised up to $\sim 13\%$ of urban specific humidity during strong inversion events in winter 2013-2014 (Gorski et al., 2015). Here we combine those data with three additional winters of water vapor isotope measurements in Salt Lake City, UT (DJF 2014-2017), allowing us to investigate relationships between meteorology, atmospheric stability, and estimated CDV amount.

20 ## 2   Methods

2.1   Estimates of Atmospheric Stratification

The SLV experiences periods of enhanced atmospheric stability each winter when cold air pools in the valley under warmer air aloft (Lareau et al., 2013; Whiteman et al., 2014). Atmospheric stratification is present when atmospheric potential temperature increases with height. Nocturnal stratification is common in many settings due to more rapid radiative cooling near the surface than aloft, but the SLV and other mountain basins can experience periods of extended atmospheric stability lasting longer than

25 a diurnal cycle (Lareau et al., 2013; Whiteman et al., 2001, 1999). These periods are commonly referred to as persistent cold air pools (PCAPs) (Gillies et al., 2010; Green et al., 2015; Malek et al., 2006).

We assess large-scale SLV vertical stability using twice-daily atmospheric sounding data from the Salt Lake City Airport (KSLC, 0Z and 12Z, or 5 and 17 MST). Sounding profiles were obtained from the Integrated Global Radiosonde Archive

30 (IGRA) (Durre and Yin, 2008), and interpolated to 10 m resolution between the surface (~ 1290 m) and 5,000 m. We calculate two metrics of atmospheric stability from the radiosonde data: a bulk valley heat deficit and an estimated mixing height. The valley heat deficit is the energy that must be added between the surface and some height to bring this portion of the atmosphere to the dry adiabatic lapse rate (e.g., $\frac{\partial \theta}{\partial z} = 0.0 \, \mathrm{K \, km^{-1}}$ or $\frac{\partial T}{\partial z} = -9.8 \, \mathrm{K \, km^{-1}}$). Valley heat deficit ($VHD$) is calculated following

prior studies of winter stability in the SLV (Baasandorj et al., 2017; Whiteman et al., 2014):

$$VHD = c_p \sum_{1290 \text{ m}}^{2200 \text{ m}} \rho(z)[\theta_{2200 \text{ m}} - \theta(z)]\Delta z \qquad (1)$$

where c_p is the specific heat capacity at constant pressure for dry air (1005 J kg^{-1} K^{-1}), $\rho(z)$ is the air density as a function of height (kg m^{-3}), $\theta_{2200 \text{ m}}$ and $\theta(z)$ are the potential temperatures at 2200 m above sea level and at height z respectively

5 (K), and Δz is the thickness of each layer (10 m). Following Whiteman et al. (2014), we define a PCAP as three or more consecutive soundings with a $VHD >$4.04 MJ m^{-2}.

Mixing heights are estimated from sounding data, with the method used depending on whether a surface-based temperature inversion (SBI) is present or absent. If the sounding features an SBI, the mixing height is estimated as the height at the top of the SBI (Bradley et al., 1993). If there is no SBI, the mixing height is estimated using a bulk Richardson number method

10 (Vogelezang and Holtslag, 1996; Seidel et al., 2012). The bulk Richardson number, which is a measure of the ratio of buoyancy to shear production of turbulence, is calculated as:

$$Ri(z) = \frac{(g/\theta_{vs})(\theta_v(z) - \theta_{vs})(z - z_s)}{(u(z) - u_s)^2 + (v(z) - v_s)^2 + bu_*^2} \qquad (2)$$

where $Ri(z)$ is the bulk Richardson number as a function of height, g is the acceleration due to gravity (9.81 m s^{-2}), θ_v is the virtual potential temperature (K), z is the altitude (m above sea level), u and v are the zonal and meridional wind components

15 (m s^{-1}), and bu_*^2 is the effect of surface friction. A subscript 's' indicates these are surface values. As u_* is not available from radiosonde observations, we assumed frictional effects were negligible (Seidel et al., 2012). This assumption is particularly well justified during stable atmospheric conditions (Vogelezang and Holtslag, 1996), such as during PCAPs. The mixing height was identified as the lowest altitude where $Ri(z)$ was greater than a critical value of 0.25.

2.2 Water Vapor Isotope Data

20 Water vapor isotope data were collected from a Picarro L2130-i water vapor isotope analyzer. Vapor was sampled from the roof of the eight-story (~ 35 m above the ground) William Browning Building (WBB, 40.7662°N, 111.8458°W, 1440 m above sea level) on the University of Utah campus through copper (prior to winter 2016/2017) or teflon tubing, using a diaphragm pump operating at ~ 3 L min^{-1}. Standards were analyzed every 12 hours using the Picarro Standards Delivery Module (SDM), using lab air pumped through a column of anhydrous calcium sulfate (Drierite) as a dry gas source.

25 We calibrated the data using the University of Utah vapor processing scripts, version 1.1. Calibration of raw instrument values at ~ 1 Hz on the instrument scale to hourly averages on the VSMOW scale proceeds across three stages (following Gorski et al., 2015): (1) Measured isotope values are corrected for an apparent dependence on cavity humidity, using correction equations developed by operating the SDM at a range of pumping rates. (2) A background humidity correction is performed to account for incomplete drying of lab air by the drying agent. We assume that 250 ppm of water vapor passes through the drying column

30 and that the water vapor passing through the column has the same isotopic composition as the ambient air measured for the 5 minutes immediately prior to standards measurements (e.g., fractionation by the drying column is negligible). (3) Analyzer

measurements are calibrated to the VSMOW-VSLAP scale using two standards of known isotopic composition delivered by the SDM, using calibration periods that bracket a series of ambient vapor measurements.

2.3 CO_2 and meteoroogical measurements

Meteorological measurements were co-located with water vapor isotope sampling on the roof of the WBB. Temperature, humidity, wind speed, solar radiation, and pressure measurements are all made at 5-min averages (Horel et al., 2002), and were averaged to 1 hour blocks for analysis.

CO_2 measurements were made in two different locations during the study period. Prior to August 2014, CO_2 measurements were made on the roof of the Aline Skaggs Biology Building (ASB) on the University of Utah campus, $\sim 0.25\,\mathrm{km}$ south of the WBB. CO_2 and H_2O measurements made at ASB were performed using a Li-Cor 7000. Atmospheric air was drawn through a 5 L mixing volume and measured every five minutes. Pressure and H_2O dilution corrections were applied by the Li-Cor. All measurements were recorded to a Campbell Scientific CR23X.

From August 2014 onwards, CO_2 measurements have been made at the WBB where they are co-located with the water vapor isotope and meteorological measurements described in section 2.2. Atmospheric CO_2, CH_4 and H_2O measurements were performed using a Los Gatos Research Off-Axis Integrated Cavity Output Spectroscope (Model 907-0011, Los Gatos Research Inc., San Jose, CA). Measurements were recorded at 0.1 Hz. The effects of water vapor dilution and spectrum broadening (Andrews et al., 2014) were corrected by LGR's real-time software, and were independently verified through laboratory testing.

At both ASB and WBB, calibration gases were introduced to the analyzer every three hours using three whole-air, dry, high-pressure reference gas cylinders with known CO_2 concentrations, tertiary to the World Meteorological Organization X2007 CO_2 mole fraction scale (Zhao and Tans, 2006). Concentrations of the calibration gases spanned the expected range of atmospheric observations. Each standard of known concentration is linearly interpolated between two consecutive calibration periods to represent the drift in the averaged measured standards over time. Ordinary least squared regression is then applied to the interpolated reference values during the atmospheric sampling periods to generate a linear slope and intercept. These are then used to correct all uncalibrated atmospheric observations between calibration periods.

Seven months of overlapping data were collected at both ASB and WBB and analyzed to identify any significant difference in measurement locations. The two locations are highly similar ($CO_{2,WBB} = 0.98 CO_{2,ASB} + 8.087, r^2 = 0.96$), though pollutants appear to "mix-out" at the end of a PCAP event approximately one hour earlier at ASB relative to WBB.

2.4 Mixing analysis between meteorological humidity and CDV

CDV can be detected by using a two-part isotopic mixing model that treats meteorological or advected vapor and CDV as the end members. We develop a schematic demonstrating the 'natural' evolution of d-excess under atmospheric moistening and condensation conditions, as well as through moistening via the addition of CDV. The isotopic composition of an air parcel

losing moisture in a Rayleigh condensation process can be modeled as (Gat, 1996):

$$\delta = \left[\left(\delta_0 + 1 \right) \left(\frac{q}{q_0} \right)^{\alpha - 1} - 1 \right] \tag{3}$$

where δ is the isotopic composition, q is the specific humidity, and α is the temperature-dependent equilibrium fractionation factor between vapor and the condensate. A subscript zero indicates the initial conditions of a parcel prior to condensation.

5 Humidity is removed from the air parcel through adiabatic cooling starting from the parcel's initial dew point temperature and cooling in 0.5 K intervals to 243 K; progressive cooling is used to account for changes in α with temperature. $\delta^{18}O$ and δ^2H are modeled separately and then combined to estimate the evolution of d-excess throughout condensation. We used fractionation factors for vapor over liquid for temperatures above 273 K (Horita and Wesolowski, 1994) and for vapor over ice for temperatures below 253 K (Majoube, 1970; Merlivat and Nief, 1967). We interpolated α values between 273 K and 253

10 K to account for mixed-phase processes between these temperatures. As the heavy isotopes of both oxygen and hydrogen are progressively removed through condensation, d-excess increases as humidity is decreased, approaching a limit of 7000‰ if all ^2H and ^{18}O were removed (Bony et al., 2008).

We also modeled the isotopic evolution of d-excess in an air parcel in the absence of CDV experiencing mixing between the moist and dry end members of the Rayleigh distillation curve. D-excess is modeled throughout this humidity range as a

15 mass-weighted mixing model average of the d-excess values of both end members:

$$d_{mix} = \frac{d_{dry}q_{dry} + d_{moist}q_{moist}}{q_{dry} + q_{moist}} \tag{4}$$

Likewise, moistening of the lower troposphere by CDV can be modeled as a mixing process between CDV and the background "natural" water vapor:

$$d_{mix} = \frac{d_{CDV}q_{CDV} + d_{bg}q_{bg}}{q_{mix}} \tag{5}$$

20 where subscripts CDV, bg, and mix refer to properties of CDV, the atmospheric moisture in the absence of CDV, and values of the mixed parcel, respectively. Gorski et al. (2015) assumed a mean value of -225‰ for d_{CDV} based on a few direct measurements of CDV. Adopting this value, we construct a model framework to explain changes in d-excess relative to humidity expected from natural condensation and mixing pathways as well as the addition of moisture via CDV (Fig. 1), but also revisit this assumption based on further analysis of our data (below). Drying the atmosphere by mixing in a dry air mass in the absence

25 of CDV or by Rayleigh condensation increases the d-excess of ambient vapor, whereas atmospheric moistening occurring due to mixing with a moist air mass can decrease the d-excess of ambient vapor. The response of d-excess due to these natural processes is non-linear with respect to changes in humidity, and very similar between condensation and mixing of "natural" air masses (Fig. 1). In contrast, small mass additions of CDV (up to 500 ppm) produce a strong, quasi-linear decrease in d_{mix} with increasing q_{CDV} (Fig. 1). Deviation from the "natural" air mass mixing line is greatest at low q_{bg} for a given q_{CDV}, as CDV

30 comprises a larger fraction of q_{mix}.

Finally, recasting these mixing-model equations following Miller and Tans (2003), we can estimate d_{CDV} using a Keeling-style approach (1958; 1961). In this framework, the product of d_{obs} and q_{obs} is proportional to q_{CDV}:

$$d_{obs}q_{obs} = d_{CDV}q_{CDV} + d_{bg}q_{bg} \tag{6}$$
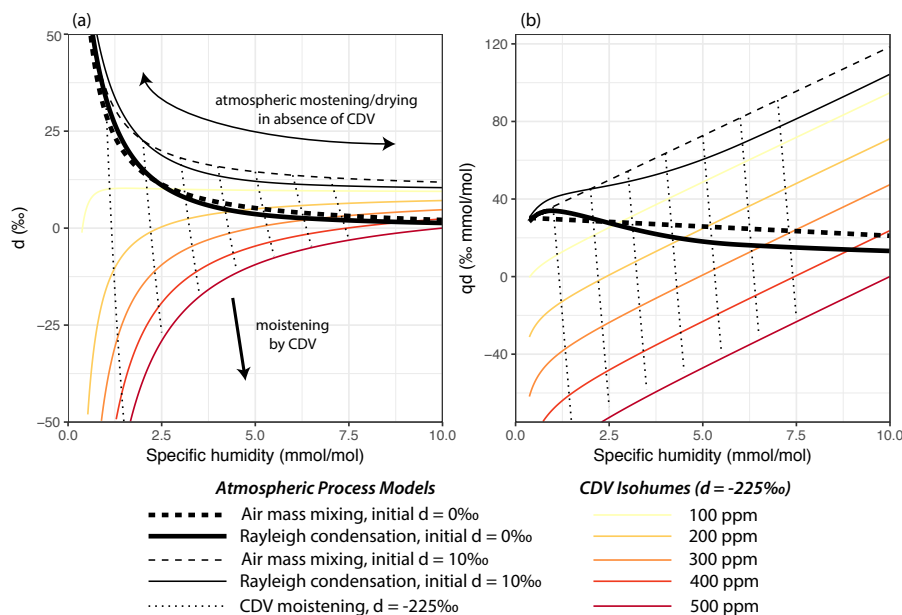
Figure 1. Schematic of expected changes in the d-excess of atmospheric vapor with changes in humidity associated with atmospheric moistening and drying in the absence of CDV due to Rayleigh distillation (solid black lines) or air mass mixing (dashed black lines) or the addition of CDV (dotted black lines). Models for Rayleigh distillation and air mass mixing are shown for two initial d-excess values of the moist end member: 0‰ (thin lines) and 10‰ (thick lines). Panel (a) shows this relationship of d (‰) vs specific humidity, q (mmol mol^{-1}), where mixing processes trace hyperbolic pathways, and panel (b) shows the same models but with axes of qd (‰ mmol mol^{-1}) against q (mmol ^{m}ol^{-1}), where mixing processes are linear. Finally, lines across a yellow-to-red gradient are drawn to show the impact of fixed amounts of CDV addition ranging from 100 ppm (yellow) to 500 ppm (red) as a function of specific humidity.

If we assume that q_{CDV} is linearly related to the increase in CO_2 above background concentrations, d_{CDV} can be estimated as the slope of a linear regression between dobsqobs and observed CO_2 concentrations:

$$d_{obs}q_{obs} = d_{CDV}(ef)[CO_2 - \min(CO_2)] + d_{bg}q_{bg} \tag{7}$$

where ef is the emissions factor, which is the stoichiometric ratio of H_2O to CO_2 in combustion products, and $[CO_2 -$
5 $\min(CO_2)]$ represents the amount of excess CO_2 in the atmosphere above the background value. We define the background CO_2 value to be the seasonal minimum value observed at the WBB or the ASB. We apply two linear mixed models where the intercept is treated as a random factor to estimate d_{CDV}: in the first, year-to-year variability is treated as a random effect, while in the second, PCAP-to-PCAP event-scale variability is treated as a random effect. These models are constructed to find the best-fit slope, and therefore the best-fit estimate of d_{CDV}, across all PCAP events. As a result, they implicitly assume that
10 changes in d_{CDV} through time are small compared to changes in $d_{bg}q_{bg}$, or that changes in the emissions profile and components of SLV are small compared to environmental variability in humidity and d-excess.
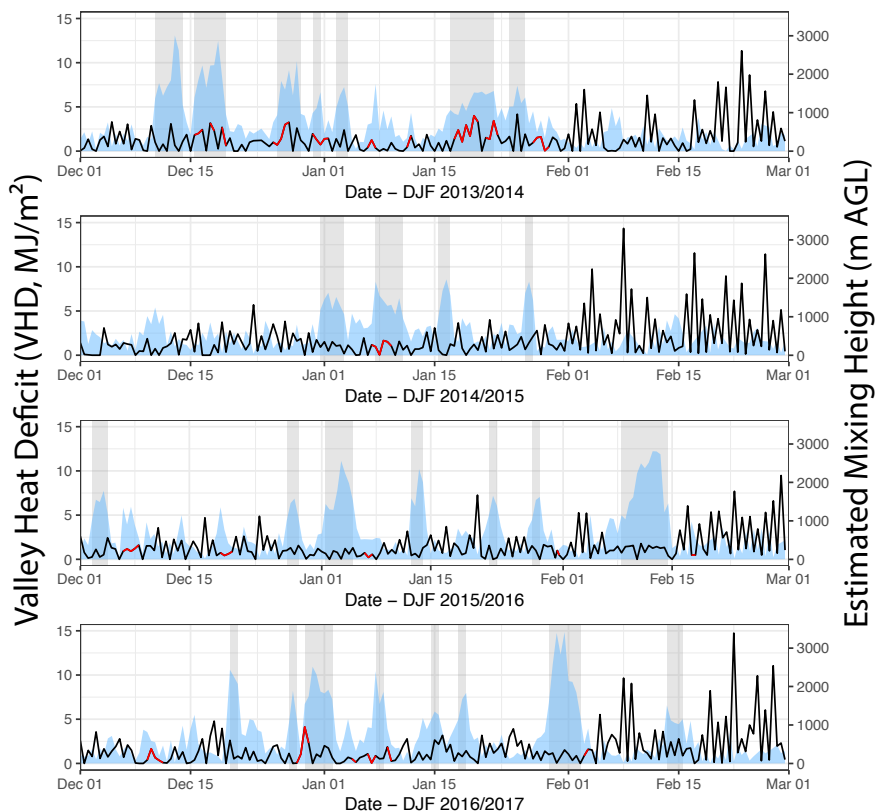
Figure 2. Valley heat deficit ($MJ\,m^{-2}$, blue polygon) and mixing height (m, black indicates Richardson mixing height; red indicates surface-based inversion top) by season. Seven, four, seven, and eight PCAP events are identified for DJF 13/14, 14/15, 15/16, and 16/17, and are denoted by light gray shading.

3 Results

We observed 26 PCAP events across four winters, with seven, four, seven, and eight occurring during DJF 13/14, 14/15, 15/16, and 16/17, respectively (Fig. 2). VHD exceeded $4.04\,MJ\,m^{-2}$ for a 30%, 18%, 27%, and 25% of the observed KSLC soundings during each winter. Variability of 1 to 2 $MJ\,m^{-2}$ between consecutive soundings is common, and results from

5   the diurnal cycle of surface heating during the day and radiative cooling at night (Whiteman et al., 2014). Calculated mixing heights ranged from the surface (1290 m) to 4680 m, with a median value of 1560 m. The mean mixing height and its variance are low in December and January, though both increase in February as solar radiation increases and more energy is available to grow the daytime convective boundary layer. CO_2 concentrations show close inverse associations with measured d-excess values across diurnal to synoptic timescales (Fig. 3). CO_2 concentrations and d-excess values were inversely cross-correlated

10   for all four winter periods ($r = -0.555$, -0.555, -0.497, and -0.665 for each consecutive winter). The maximum cross-correlation was observed with zero lag in DJF 14/15 and 16/17, whereas d-excess lagged CO_2 by 1 hour in DJF 13/14 and
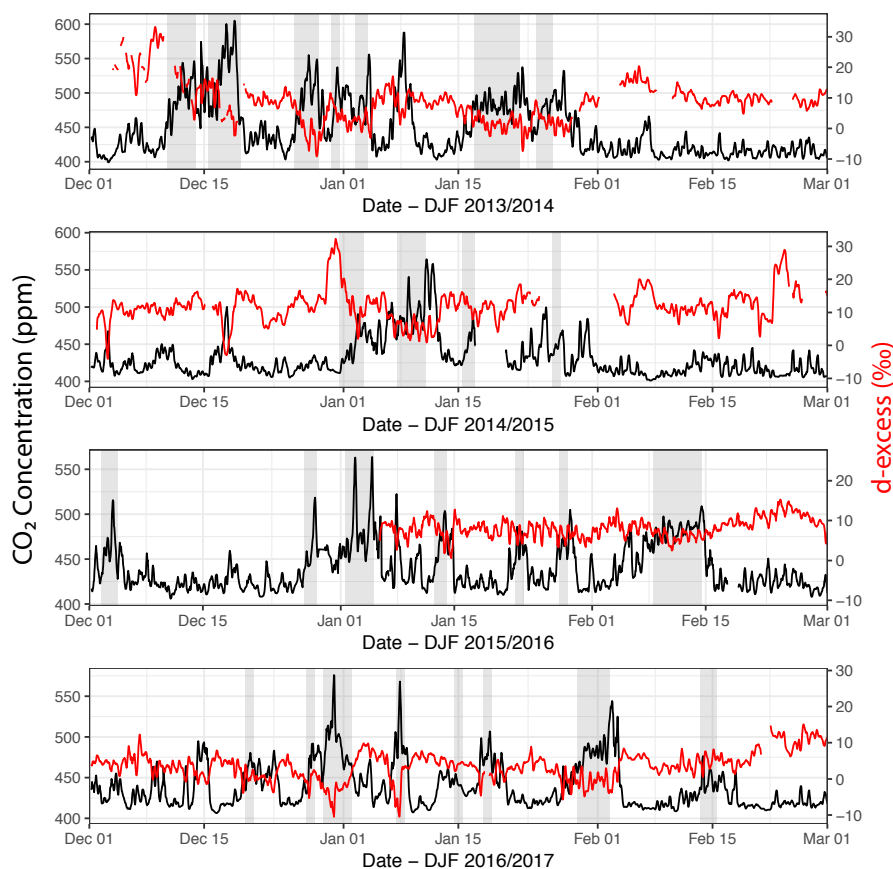
Figure 3. Six hour running-mean CO_2 concentrations (ppm, black line) and water vapor d-excess (‰ VSMOW, red line) measured at the WBB for DJF 2013-2017. Persistent cold air pool events are denoted by gray rectangles. When the lower atmosphere is stable, CO_2 builds up in the boundary layer and d-excess tends to decrease.

15/16. For each winter season, minimum/maximum hourly CO_2 concentrations were 397/637 ppm, 400/581 ppm, 404/598 ppm, 406/653 ppm, whereas minimum/maximum hourly d-excess values were $-23.8/33.9$‰, $-5.2/33.4$‰, $-3.3/17.6$‰, and $-17.6/16.1$‰. During each PCAP event, CO_2 was elevated relative to its background value. For most PCAP events, d-excess decreased commensurately with the increase in CO_2; however, several exceptions were observed. For example, PCAPs

5 in February 2016 and 2017 showed diurnal cyclicity in d-excess and CO_2, but mean concentrations through the event remained fairly stable. Additionally, elevated CO_2 and depressed d-excess values were frequently observed in the absence of PCAPs (e.g., mid-December 2014 and 2016); these cases are associated with low mixing heights, but not necessarily high VHD values.

3.1 Relationship between CO_2 and d-excess and estimating d-excess of CDV

Clear distinctions emerged in the distributions of CO_2 and d-excess during PCAP events compared to more well-mixed periods (Fig. 4). Non-PCAP periods are typically defined by lower CO_2 values, usually below 450 ppm, and a broad range of d-excess values averaging around $\sim 10‰$ and spanning $\sim 0-30 ‰$. D-excess variability during non-PCAP periods is likely controlled

5   by natural moistening and dehydration processes, including air mass mixing, Rayleigh-style condensation and evaporative inputs from the Great Salt Lake. In contrast, a strong linear relationship between CO_2 and d-excess is observed during PCAP periods, with d-excess values decreasing proportionally with increasing CO_2 (Fig. 4). At the highest CO_2 concentrations, d-excess can be >10 ‰ lower than when CO_2 is at background levels outside of PCAP events.

These relationships between "natural" moistening and drying of the boundary layer and moistening by CDV become appar-

10 ent from the relationship between d-excess and humidity (Fig. 5). Changes in d-excess and q from atmospheric moistening and drying processes in the absence of CDV are expected to follow a hyperbolic or near hyperbolic relationship, and trend toward increasing d-excess values at low humidities (Fig. 1). In contrast, addition of CDV to the atmosphere will promote strong negative deviations from this $q - d$ relationship that are proportional to amount of CDV, and are essentially linear over likely ranges of q_{CDV}. These patterns are observed in our measurements, where d-excess values are high and trend upward for low

15 humidities at low CO_2 concentrations, and show linear patterns of decrease with increasing CO_2 (Fig. 5). Strong positive d-excess excursions are observed during the first two winters, and are associated with dry, cold conditions following the passage of a strong cold front. No equivalent excursions are observed during the last two winters, perhaps due to a similar magnitude cold front event not occurring during the observed portions of those winters. Negative excursions are observed during PCAP events or when CO_2 is elevated, and can be seen across a range of humidity values.

20 We leverage the observed, coupled variability in d-excess and CO_2 during periods of enhanced CO_2 to test previous theoretical estimates and limited source measurements of d_{CDV} using a Keeling-style approach (1958; 1961). Recall that d_{CDV} can be estimated as the slope of a regression between $q_{obs}d_{obs}$ and q_{CDV}. We approximate q_{CDV} by multiplying the enrichment of CO_2 above its background value by an emissions factor, ef, which represents the stoichiometric ratio of H_2O:CO_2 in combustion products (Gorski et al., 2015). The best-fit slope of a linear mixed model allowing for random variation in the intercept be-

25 tween PCAP events yields an estimate of d_{CDV} of $-308 \pm 12‰$ for $ef = 1.0$ and $-154 \pm 6‰$ for $ef = 2.0$ (Fig. 6). A similar model, allowing the intercept to vary by season instead of by event, yields comparable estimates of d_{CDV} of $-250 \pm 15‰$ for $ef = 1.0$ and $-125 \pm 7‰$ for $ef = 2.0$. The former model is likely to be more robust as it better accounts for meteorological variability between events. The range of d_{CDV} estimates from these observations are consistent with theoretical models from (Gorski et al., 2015), though uncertainty in a representative value of ef across time and from the mixture of fuel sources and

30 combustion systems in the SLV prohibits a precise determination of d_{CDV}.
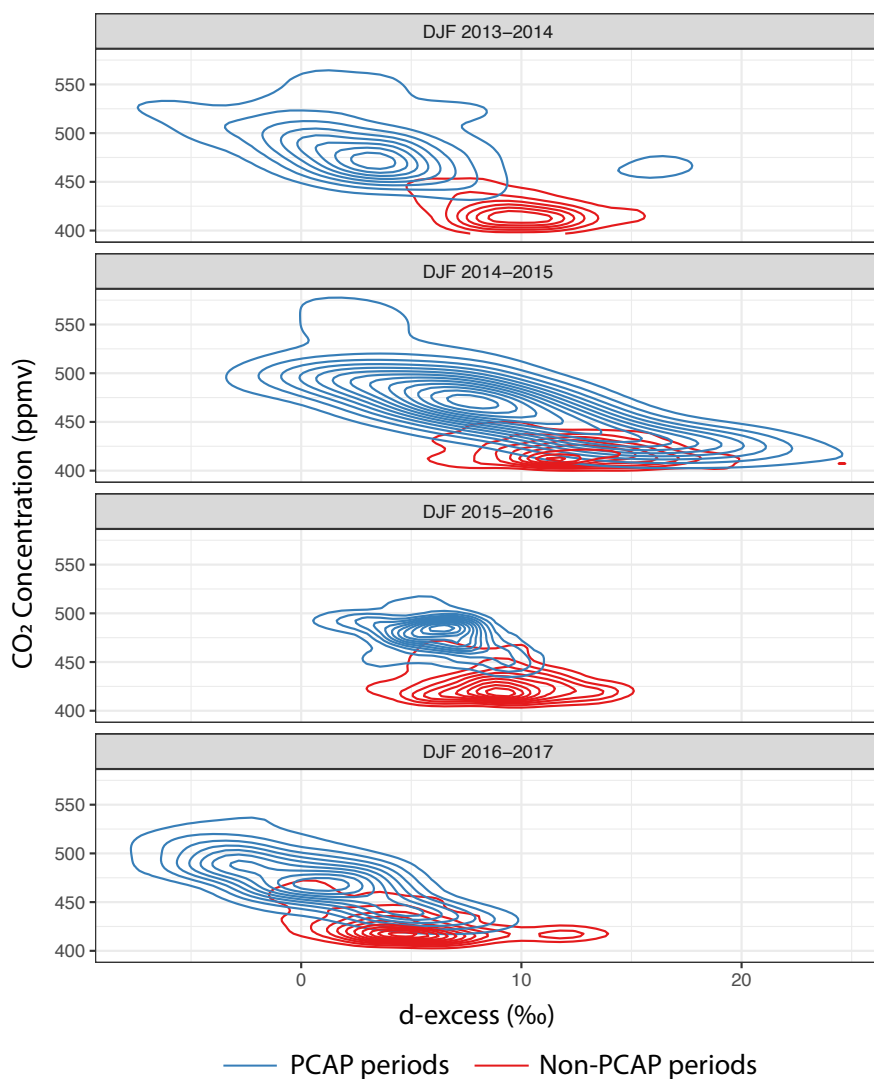
Figure 4. Distributions of CO_2 and d-excess for DJF 13/14 (first row), 14/15 (second row), 15/16 (third row) and 16/17 (fourth row). Conditions during PCAP events are shown in blue contours and non-PCAP periods are shown in red contours. Non-PCAP periods are marked by lower CO_2 concentrations (<450 ppm) and a broad range of positive d-excess values, PCAP periods show a strong linear relationship, with decreasing d-excess values associated with increasing CO_2 concentrations.
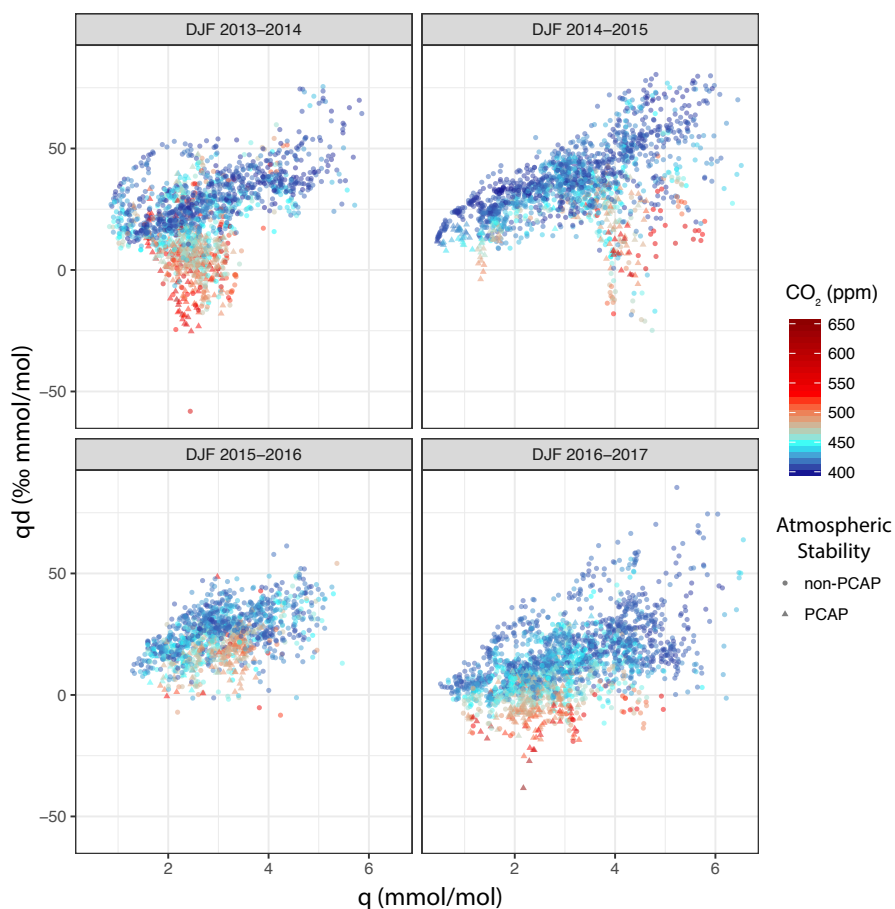
Figure 5. Relationship of the product of specific humidity and d-excess, qd (‰ mmol mol^{-1}), against specific humidity q (mmol mol^{-1}). Points are colored by CO_2 concentration (ppm) at the time of measurement, and shapes correspond to if the data point was collected during a PCAP event or outside of a PCAP event. Moistening and drying by condensation and mixing of "natural" air masses occurs along a line with positive slope, while moistening by CDV occurs along a line with negative slope.
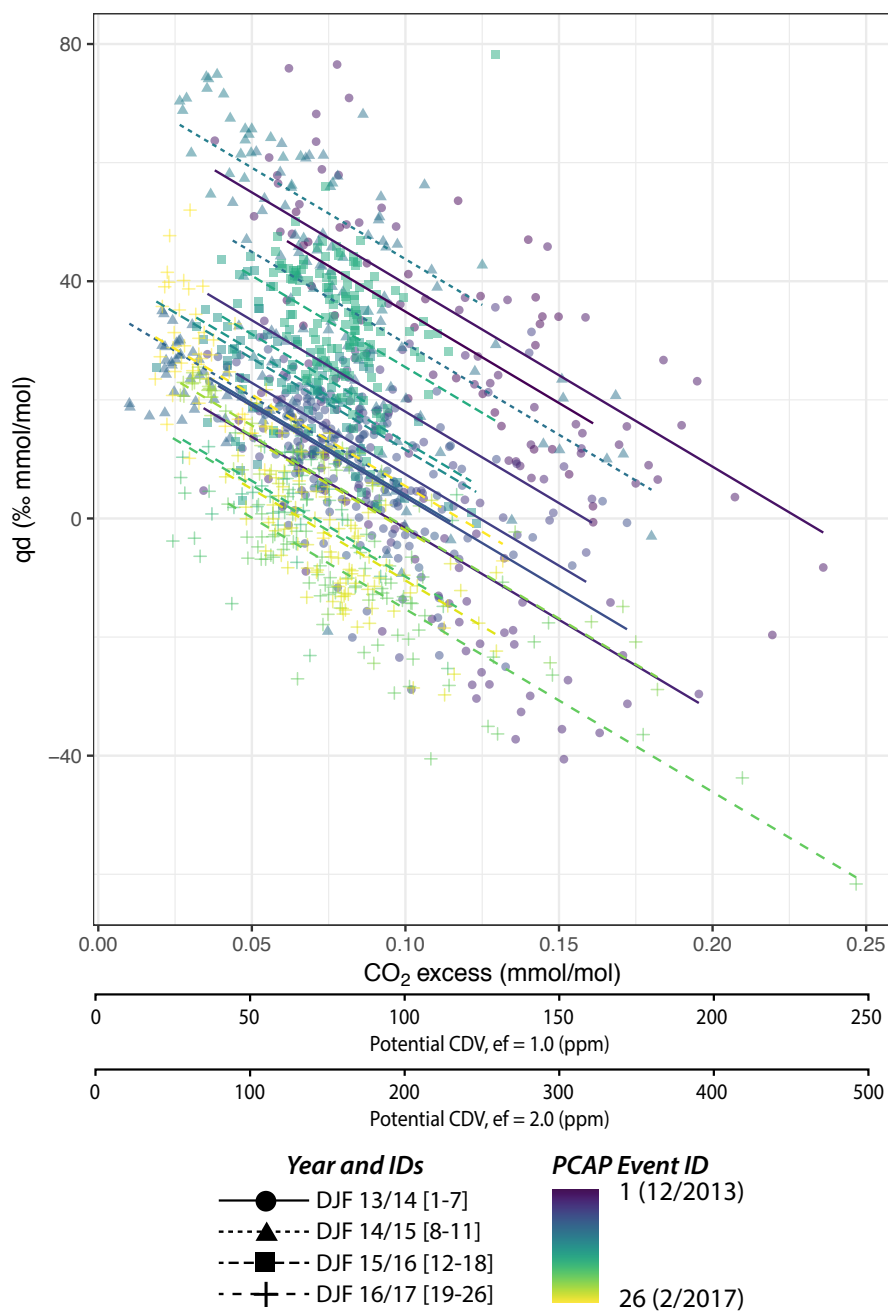
Figure 6. Keeling-style plots of qd (‰ mmol mol^{-1}) versus CO_2-excess (the difference between the observed CO_2 and the seasonal minimum CO_2) by year during PCAP events. The estimated d-excess of CDV, assuming CDV is the dominant flux of water into the boundary layer during PCAP events, is the slope of the best fit line. The best-fit linear mixed model that keeps the slope identical across years but allows for variability in the intercept is shown for each year.

3.2 Case studies

3.2.1 December 22, 2014-January 14, 2015

Two distinct PCAP events were observed between December 22, 2014 and January 14, 2015 (Fig. 7). Conditions at the beginning of this period were humid ($\sim 8 \, \mathrm{mmol \, mol^{-1}}$) and warm ($\sim 5°$ C), and both values fell rapidly to $\sim 1.75 \, \mathrm{mmol \, mol^{-1}}$ (Fig. 7b) and $-12°$ C (Fig. 7c) thorough December 30, 2014 12Z as a cold front entered the region (Fig. 7f) ahead of the first PCAP event. During this period of atmospheric drying, d-excess rose from 10‰ to >30‰ (Fig. 7a), consistent with dehydration through either a condensation process or entrainment of a dry air mass. After onset of the PCAP, however, d-excess dropped rapidly as CO_2 and CDV began to build in the valley. By January 2, CO_2 had risen to 480 ppm and d-excess had fallen to $\sim 5‰$, an increase of ~ 60 ppm and a decrease of 25‰ respectively (Fig. 7a,d). Atmospheric d-excess through this period closely followed model expectations of moistening via CDV (Fig. 7a). After the end of the first PCAP event, specific humidity and temperature rose daily until the start of the second PCAP on January 7 12Z (Fig. 7ab). During this period in between PCAP events, CO_2 remained elevated, and exhibited diurnal variability of 20-40 ppm (Fig. 7c). Changes in d-excess were consistent with diurnal cycles in d-excess driven by CDV inputs superimposed on a longer-term moistening trend (Fig. 7d). Despite the VHD falling below the PCAP threshold in between PCAP events (Fig. 2), the lower atmosphere did not become well-mixed. Airport soundings indicated an elevated inversion atop a saturated cloud layer remained during this period, which decreased surface solar heating (Fig. 7e) while wind speeds remained low (Fig. 7f). As a result, CO_2 concentrations did not return to background values (Fig. 7d). The second PCAP event, spanning January 7 12Z until January 11 00Z, was marked by prominent diurnal cycles in humidity, temperature, and CO_2 (Fig. 7a-c). Strong diurnal cyclicity was also observed in d-excess (Fig. 7d). Humidity additions were most likely a mixture of CDV and evaporation from the Great Salt Lake or sublimation of snowfall. The last day of the PCAP exhibited a strong decrease in solar irradiance (Fig. 7e), which likely indicated cloud development at the base of an elevated inversion, a feature typical of extended PCAP events (Baasandorj et al., 2017; Whiteman et al., 2014). CO_2 concentrations reached their maximum at the end of the PCAP event, and decreased slowly during the first diurnal cycle after the breakup of the PCAP, before mixing out nearly completely on January 12. Deuterium excess values followed changes in CO_2, remaining low but increasing with decreasing CO_2 during the first diurnal cycle, before rapidly increasing as CO_2 decreased at the end of the observation period (Fig. 7d). The spike in CO_2 at the termination of the PCAP is likely a due to the WBB's location on a topographic bench; strong stability during the PCAP may have kept the most polluted air below the WBB, which then was transported to higher altitudes as the PCAP ended.
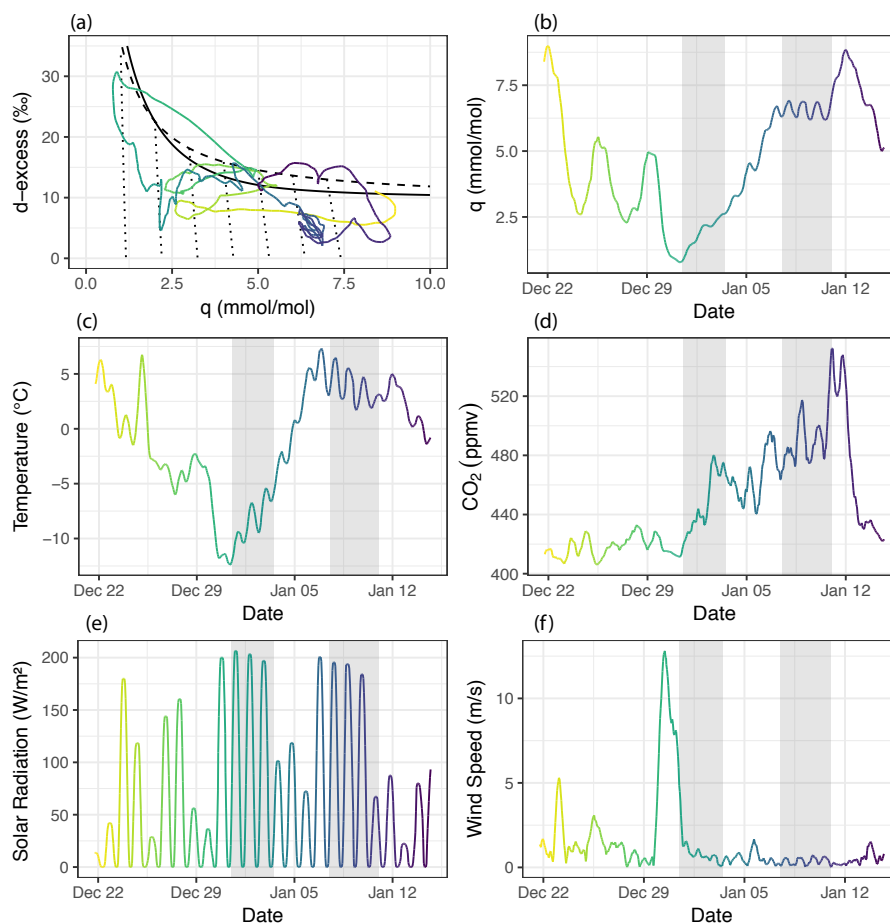
Figure 7. Relationship between d-excess and q (a) from December 22, 2014-January 14, 2015. Time series of specific humidity (b, $\mathrm{mmol\,mol^{-1}}$), temperature (c, °C), and CO_2 concentration (d, ppm) across the same time period are shown for reference, with the same color gradient used across time in all four panels. Data are plotted as 6-hour running averages.

3.2.2 February 3-17, 2016

This period was marked by one extended PCAP from February 8 12Z to February 14, 12Z (Fig. 8). Conditions prior to the PCAP were dry and cold for the first two days, before warming by $\sim 5°C$ and humidity increasing from ~ 3 to $\sim 5 \, \mathrm{mmol \, mol^{-1}}$ (Fig. 8b,c). CO_2 increased from 430 to 480 ppm during this period before decreasing back to 430 ppm (Fig. 8d). Deuterium excess

5 also decreased, but at a less rapid rate than anticipated for CDV addition, and instead, followed a path parallel to moistening by mixing of "natural" air masses (Fig. 8a). The remainder of the pre-PCAP period through the PCAP event was marked by slow, steady increases in q and CO_2, with prominent diurnal cycling in temperature, CO_2, q, and d-excess. Diurnal cyclicity was apparent in the relationship between d-excess and CO_2 as well, with periods of increasing (decreasing) CO_2 producing rapid decreases (increases) in d-excess with little change in q. These diurnal patterns are consistent with daytime growth of a

10 shallow convective boundary layer at the surface with a stable layer aloft; the same interpretation was made in prior studies of this event (Baasandorj et al., 2017). Diurnal cycle amplitudes of q, temperature, and CO_2 decreased for the second half of the PCAP (Fig. 8b-d), and co-occur with a reduction in surface solar radiation (Fig. 8e) as low-level clouds developed during the event. Superimposed on these diurnal cycles of d-excess against q, conditions became more moist across several days (Fig. 8a,d). Following termination of the PCAP, conditions became warmer and CO_2 decreased back toward its background value.

15 Humidity increased rapidly for a few days after the event before falling again. Both the moistening and drying occurred with small changes in d-excess, consistent with changes expected for changes in q in the absence of the buildup of CDV. Surface wind speeds remained low throughout this period (Fig. 8f), suggesting that removal of pollutants at the end of the PCAP was largely accomplished by vertical transport away from the surface.
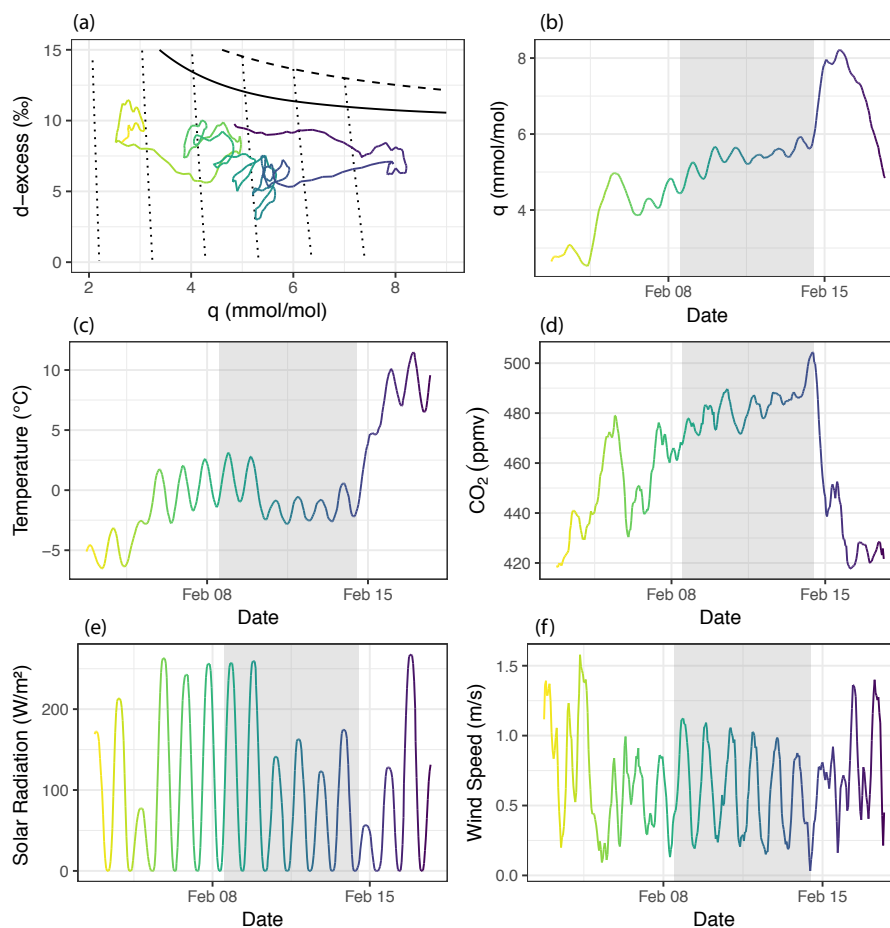
Figure 8. Relationship between d-excess and q (a) from February 1-17, 2016. Time series of specific humidity (b, $\mathrm{mmol\,mol^{-1}}$), temperature (c, $^\circ$C), and CO_2 concentration (d, ppm) across the same time period are shown for reference, with the same color gradient used across time in all four panels. Data are plotted as 6-hour running averages.

3.2.3 December 25, 2016-January 10, 2017

Three separate PCAP events occurred during the December 25, 2016 -January 10, 2017 period, at December 27 12Z to December 28 12Z, December 29 12Z to January 2 00Z, and January 7 12Z to January 8 12Z (Fig. 9). Initial conditions were humid (~ 7.5 mmol mol^{-1}), with temperatures above zero and low CO_2 concentrations (Fig. 9b-d). Ahead of the first two PCAP
5   events, temperature and humidity dropped (Fig. 9b,c), with an ~ 80 ppm increase in CO_2 following shortly after. Deuterium excess values decreased along with specific humidity prior to the first PCAP, but then decreased rapidly at the onset of the first PCAP with little change in specific humidity, likely a result of buildup in CDV associated with the increase in atmospheric CO_2 (Fig. 9a). The first and second PCAP events were separated by ~ 24 hours of decreased atmospheric stability, with a portion of the CO_2 buildup mixing out into the free troposphere (Fig. 9d). During this period, d-excess values increased as
10 CDV was presumably diluted due to mixing. As the second PCAP started, CO_2 concentrations increased by ~ 100 ppm, and d-excess values decreased by $\sim 10‰$. CO_2 fell through the latter half of the second PCAP, and mixed out to ~ 425 ppm after the termination of the PCAP; during this period, d-excess increased by $>15‰$. Diurnal variability decreases throughout the second PCAP event, likely associated with the development of low-level clouds and a reduction of solar surface heating (Fig. 9e), as noted in prior events (Fig. 7,8) (Baasandorj et al., 2017; Whiteman et al., 2014). Humidity and temperatures decreased
15 on January 5 with the passage of a second cold front, which had little impact on d-excess, but promoted strong surface cooling ahead of the third PCAP event. At the onset of the third PCAP, d-excess decreased by $>10‰$ and CO_2 increased by ~ 125 ppm. As the third PCAP ended, surface temperature, humidity, and wind speeds all increased (Fig. 9b,c,f), while CO_2 decreased (Fig. 9d) and d-excess increased (Fig. 9a), consistent with pollutants being transported out of the SLV.
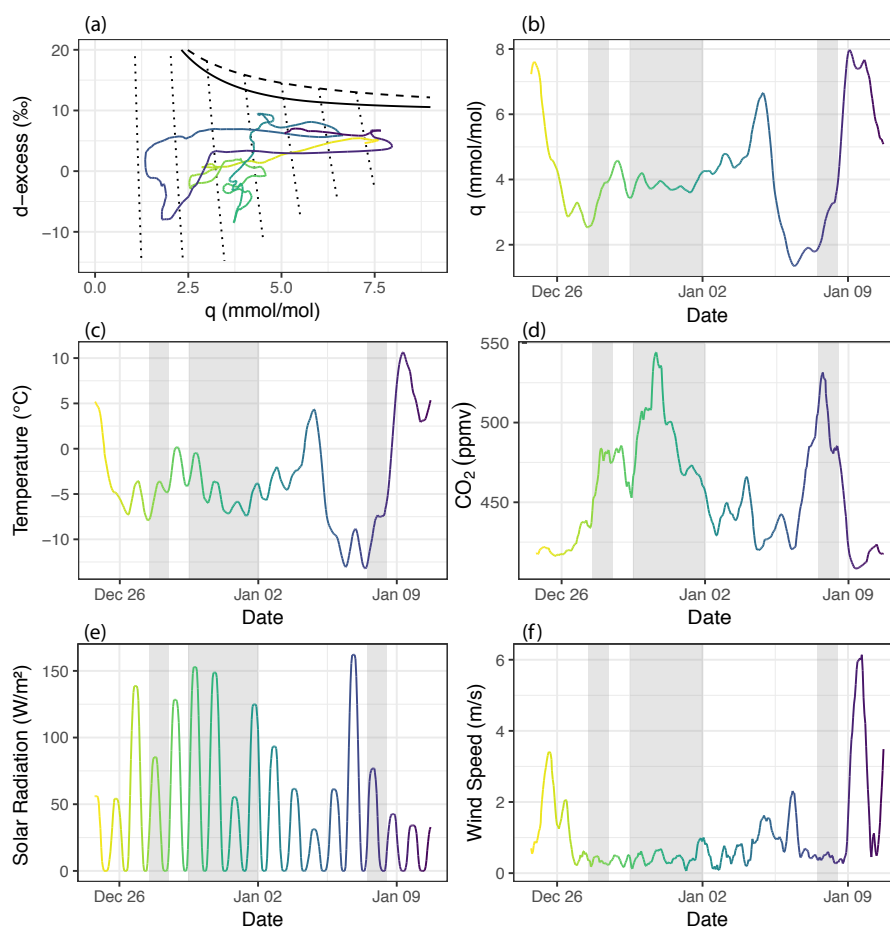
Figure 9. Relationship between d-excess and q (a) from December 25, 2016-January 10, 2017. Time series of specific humidity (b, $\mathrm{mmol\,mol^{-1}}$), temperature (c, $°C$), and CO_2 concentration (d, ppm) across the same time period are shown for reference, with the same color gradient used across time in all four panels. Data are plotted as 6-hour running averages.

3.3 Seasonal evolution of the diurnal cycle

Changes in the diurnal variability of the estimated mixing height and valley heat deficit were apparent throughout the winter season (Fig. 2). In this section, we investigate whether changes in the diurnal evolution of the mixed layer throughout the season were reflected in the ambient vapor isotope record of d-excess. Diurnal cycles of Δd-excess and ΔCO_2 varied across

5   years, months, and the presence or absence of a PCAP event, though several robust patterns emerged (Fig. 10). First, the shape of diurnal cycles of Δd-excess and ΔCO_2 were consistent, though the magnitude and timing of changes varied across month, year, and valley stability status. Δd-excess was flat or increased slightly in the early morning hours (0-6 MST), decreased throughout the morning until ~11 MST, increased from 11 MST until late afternoon (~17 MST), and then decreased again from 17 MST until late evening (Fig. 10a-i). Patterns in Δd-excess diurnal cycles mirrored ΔCO_2 patterns. Daily minimums

10   in CO_2 mirror daily maximums in d-excess, and occurred during the period of the day expected to have the most developed boundary layer and greatest exchange between the near-surface atmosphere and the free troposphere (Fig. 10j-r). Broadly, the amplitude of these cycles was greater in January than in December and February and during PCAP events across the season. Across the entire time series, the amplitude of the d-excess and CO_2 diurnal cycles were $\sim 4‰$ and $30\,\mathrm{ppm}$ respectively during January (Fig. 10b, k), but were closer to $\sim 3‰$ and $20\text{-}25\,\mathrm{ppm}$ during December (Fig. 10a,j) and February (Fig. 10c,l). During

15   PCAP events, average diurnal cycle amplitudes for d-excess and CO_2 increased to $\sim 6‰$ and $>50\,\mathrm{ppm}$ across all months (Fig. 10d-f, m-o). Conversely, outside of PCAP events, the amplitude of diurnal cycles decreased, presumably because CO_2 and CDV were mixed away from the surface more efficiently and therefore did not become concentrated near the surface.

Interannual variability in the diurnal cycles was small, with a few exceptions. For example, composite diurnal cycles for PCAP events varied the most across years (Fig. 10d-f, m-o). However, given the episodic nature of PCAPs, these diurnal

20   cycles can often be determined by 1 or 2 events in a given year. Though a consistent pattern emerged across many PCAP events, individual events were expressed differently in both the CO_2 and d-excess records.
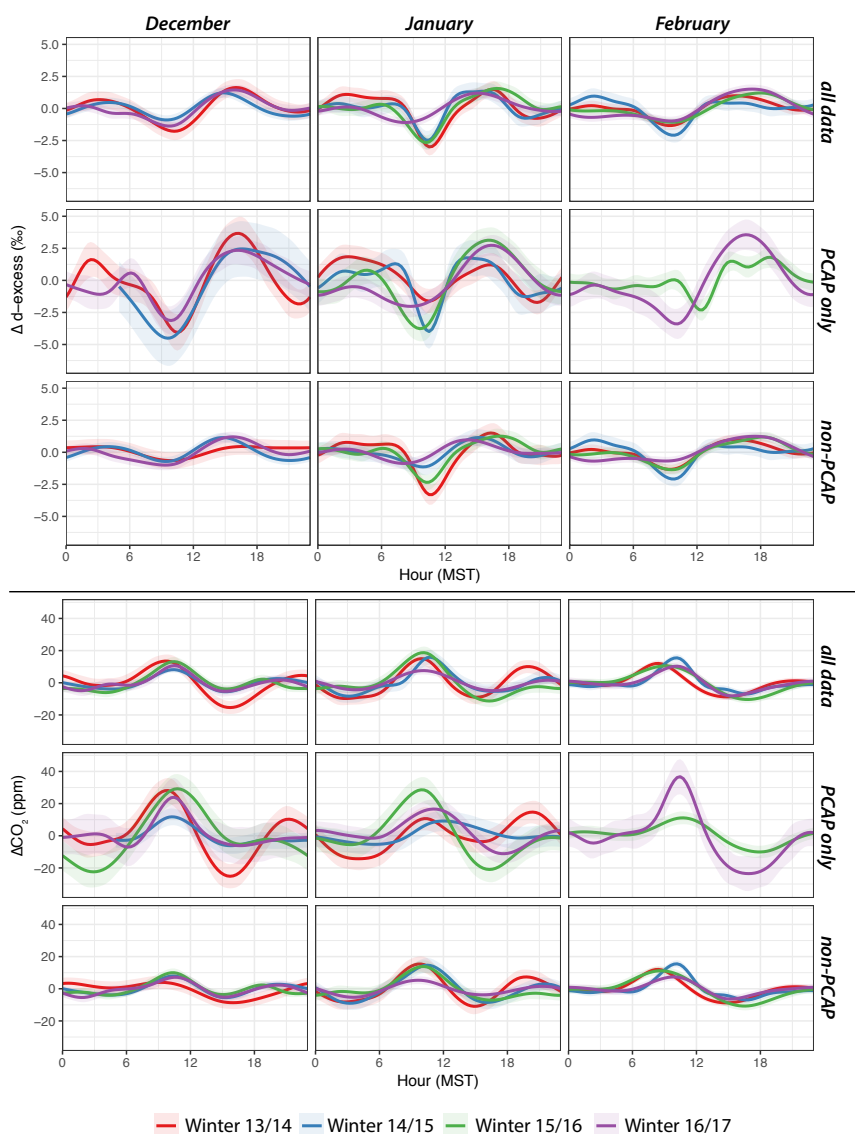
Figure 10. Diurnal cycles of Δd-excess (top half) and ΔCO_2 (bottom half) by month. The left, center, and right columns correspond to December, January, and February. Within the top and bottom halves, there are three rows corresponding to all of the observational data, PCAP periods only, and non-PCAP periods only. Mean diurnal cycle (solid lines) and uncertainty (as the standard error) are plotted for each year as different colors, and are generated from a GAM using cubic cyclic smoothing splines. Diurnal cycles are modeled as the mean deviation between the hourly time series and its 24-hour moving average. The influence of CDV in the diurnal cycle is apparent from comparing Δd-excess and CO_2 cycles: increases in CO_2 co-occur with decreases in d-excess during the early morning and late afternoon periods.

4 Discussion

CDV is evident across sub-diurnal to multi-day timescales in the Salt Lake City d-excess record. On short timescales, periods of high emission intensity near or transport to the WBB were apparent in the diurnal cycles of d-excess and CO_2. Decreases in d-excess were coincident with increases in CO_2, and occur during the morning and late afternoon when emissions were likely high and tropospheric mixing was low. Average diurnal cycles in d-excess and CO_2 showed little change overnight outside of PCAP events (Fig. 10), which was unexpected as heating emissions continued throughout the evening. The absence of overnight d-excess and CO_2 changes was likely a result of the WBB's location on a topographic bench away from large residential areas, or due to injection of cleaner air from above if a SBI occurs at an elevation below the WBB. On longer timescales, the impact of CDV was most apparent during PCAP events, where CO_2 and CDV persist in the urban atmosphere while the atmosphere in the SLV remained sufficiently stable. Some contrasts in the expression of CDV and CO_2 were apparent across the winter season and likely resulted from changes in insolation and the mechanisms resulting in stability of the near-surface atmosphere. For example, the most rapid increases in CO_2 and decreases in d-excess were observed during December and January (Fig. 3, 7, 8), when surface insolation was lower. In contrast, rapid changes were less common during February, as higher insolation can drive higher mixing heights (Fig. 2), and mix out a greater proportion of daily emissions. As a result, changes in d-excess and CO_2 exhibited large diurnal cycles superimposed upon slower synoptic trends during February PCAP events (Fig. 9).

Based on changes in d-excess relative to CO_2 during PCAP events, we have estimated the mean d-excess of CDV to be between $-125‰$ and $-308‰$. One assumption of the model used here is that all of the change in d-excess is driven by addition of CDV; other sources of vapor to the near surface, such as sublimation of snow or water evaporated from the Great Salt Lake, may introduce bias into these estimates. However, both of these sources would have less negative d-excess values, and therefore, if other sources of vapor contribute significantly to d-excess change, our estimates of d_{CDV} are a maximum estimate. The wide range of estimated CDV compositions arises from uncertainties in the representative stoichiometric ratio between H_2O and CO_2 in combustion products (e.g., ef). In principle, ef can be constrained through a detailed accounting of emissions or fuel sources (e.g., Patarasuk et al., 2016), but heat exchangers designed to improve heating efficiency may reduce the H_2O concentration in emissions, and potentially alter d_{CDV} as well through condensation (Fig. 1). Additionally, the portfolio of fuels contributing to CDV change in both time and space, and respond to meteorological conditions. For example, colder conditions increase demand for heating, which may shift the portfolio of fuel sources toward natural gas (e.g., Pataki et al., 2006). Finally, d_{CDV} can be altered by the temperature and degree of equilibration of ^{18}O between H_2O and CO_2 in combustion exhaust. If no equilibration occurs between H_2O and CO_2, the $\delta^{18}O$ values of both species should be equal to atmospheric oxygen, $23.9‰$ (Barkan and Luz, 2005; Gorski et al., 2015). In contrast, equilibration between H_2O and CO_2 will lower the $\delta^{18}O$ value of H_2O; at $100°$, for example, the $\delta^{18}O$ value of H_2O will be $\sim 29‰$ lower than the $\delta^{18}O$ of CO_2 for complete equilibration (Friedman and O'Neil, 1977; Gorski et al., 2015). The degree of equilibration appeared to vary across fuels and combustion systems (Horváth et al., 2012), which introduced uncertainty into the $\delta^{18}O$ and subsequently d of CDV. Regardless, the highly negative estimated isotopic composition of the flux into the boundary layer during PCAP events, which we have assumed is predominantly CDV, precludes other potential sources of water vapor apart from CDV from explaining

the observed isotopic change. Further refinements in CDV determination with stable water vapor isotopes may provide an additional tool with which to measure fossil fuel emissions and verify emissions reductions.

Though the most prominent periods of CO_2 and CDV buildup occur during PCAP events, decreases in d-excess coincident with increases in CO_2 were apparent across shorter timescales as well. CO_2 and CDV from emissions built up in the boundary layer whenever atmospheric stability was present regardless of whether VHD values were high enough to qualify as a PCAP. For a given quantity of fuel burned, CO_2 increases and CDV concentrations will be higher if the mixed height is lower because the volume these species can mix into is smaller. Despite this, we saw no robust relationship between CDV or CO_2 and our mixing height estimates. Atmospheric soundings at the Salt Lake City airport occurred at 5 and 17 MST, however, and were unlikely to capture diurnal extremes in the mixing height. Mid-afternoon patterns in the diurnal cycles of d-excess and CO_2 suggested that boundary layer development and entrainment did mix a fraction of combustion products out of the boundary layer, even during PCAP events (Fig. 10). In contrast, CO_2 and CDV build to higher concentrations during the early morning and late afternoon (Fig. 10), when boundary layer mixing was decreased and emissions were likely higher.

5 Conclusions

Measurements of ambient vapor d-excess were paired with CO_2 observations across four winters in Salt Lake City, UT. We found a strong negative association between CO_2 and d-excess on sub-diurnal to seasonal timescales. Elevated CO_2 and CDV was most prominent during PCAP periods, where atmospheric stability was high for extended periods. We outline theoretical models that can discriminate between changes in d-excess driven by condensation, advection, and mixing processes the "natural" hydrological cycle and those driven by CDV moistening. CDV is most detectable when humidity is low, as CDV likely comprises a larger fraction of total humidity and the anticipated signal between vapor with and without CDV is large. Our estimates of $-308‰$ to $-125‰$ for d_{CDV} are consistent with theoretical constraints and a limited number of direct observations of CDV (Gorski et al., 2015), though the range remains large due to uncertainties in a valley-scale stoichiometric ratio of H_2O and CO_2 and the degree of isotopic equilibration between H_2O and CO_2 in emissions. These estimated compositions, however, do suggest a significant role for CDV during PCAP events, particularly during periods where there was a large isotopic change, but little change in humidity. Prominent diurnal cycles were observed in both d-excess and CDV that could be tied to both emissions intensity and atmospheric processes. Further refinements of these methods may help apportion humidity changes during the winter between CDV and different advected "natural" water sources to the urban environment, and help verify emissions amounts and/or emissions reductions.

Code and data availability. IGRA radiosonde data are available from https://www.ncdc.noaa.gov/data-access/weather-balloon/integrated-global-radiosonde-archive. WBB meteorological measurements are available for download from mesowest.utah.edu, and CO_2 data are available at air.utah.edu. Calibrated WBB isotope data products are available from the Open Science Framework (osf.io/ekty3), and codes used to calibrate the water isotope analyzer measurements are available from GitHub (https://github.com/rfiorella/UU_vapor_processing_scripts/tree/v1.1.0)

Competing interests. The authors declare that they have no conflicts of interest.

Acknowledgements. RPF and GJB received support from NSF grant EF-1241286. RB, JCL, and the CO_2 measurements were supported by grants from Department of Energy (DOE) grant DESC0010624 and the National Oceanic and Atmospheric Administration (NOAA) grant NA140AR4310178.

References

Andrews, A. E., Kofler, J. D., Trudeau, M. E., Williams, J. C., Neff, D. H., Masarie, K. A., Chao, D. Y., Kitzis, D. R., Novelli, P. C., Zhao, C. L., Dlugokencky, E. J., Lang, P. M., Crotwell, M. J., Fischer, M. L., Parker, M. J., Lee, J. T., Baumann, D. D., Desai, A. R., Stanier, C. O., De Wekker, S. F. J., Wolfe, D. E., Munger, J. W., and Tans, P. P.: CO2, CO, and CH4 measurements from tall towers in the NOAA earth system research laboratory's global greenhouse gas reference network: Instrumentation, uncertainty analysis, and recommendations for future high-accuracy greenhouse gas monitoring efforts, Atmospheric Measurement Techniques, 7, 647–687, https://doi.org/10.5194/amt-7-647-2014, 2014.

Baasandorj, M., Hoch, S. W., Bares, R., Lin, J. C., Brown, S. S., Millet, D. B., Martin, R., Kelly, K., Zarzana, K. J., Whiteman, C. D., Dube, W. P., Tonnesen, G., Jaramillo, I. C., and Sohl, J.: Coupling between Chemical and Meteorological Processes under Persistent Cold-Air Pool Conditions: Evolution of Wintertime PM2.5 Pollution Events and N2O5 Observations in Utah's Salt Lake Valley, Environmental Science and Technology, 51, 5941–5950, https://doi.org/10.1021/acs.est.6b06603, 2017.

Barkan, E. and Luz, B.: High precision measurements of 17O/16O and 18O/16O ratios in H2O, Rapid Communications in Mass Spectrometry, 19, 3737–3742, https://doi.org/10.1002/rcm.2250, 2005.

Bergeron, O. and Strachan, I. B.: Wintertime radiation and energy budget along an urbanization gradient in Montreal, Canada, International Journal of Climatology, 32, 137–152, https://doi.org/10.1002/joc.2246, 2012.

Blossey, P. N., Kuang, Z., and Romps, D. M.: Isotopic composition of water in the tropical tropopause layer in cloud-resolving simulations of an idealized tropical circulation, Journal of Geophysical Research Atmospheres, 115, 1–23, https://doi.org/10.1029/2010JD014554, 2010.

Bony, S., Risi, C., and Vimeux, F.: Influence of convective processes on the isotopic composition (δ18O and δD) of precipitation and water vapor in the tropics: 1. Radiative-convective equilibrium and Tropical Ocean-Global Atmosphere-Coupled Ocean-Atmosphere Response Experiment (TOGA-COARE), Journal of Geophysical Research Atmospheres, 113, 1–21, https://doi.org/10.1029/2008JD009942, 2008.

Bradley, R. S., Keimig, F. T., and Diaz, H. F.: Recent Changes in the North American Artic Boundary Layer in Winter, https://doi.org/10.1029/93JD00311, 1993.

Dansgaard, W.: Stable isotopes in precipitation, Tellus, 16, 436–468, https://doi.org/10.3402/tellusa.v16i4.8993, https://www.tandfonline.com/doi/full/10.3402/tellusa.v16i4.8993, 1964.

Duren, R. M. and Miller, C. E.: Measuring the carbon emissions of megacities, Nature Climate Change, 2, 560–562, https://doi.org/10.1038/nclimate1629, http://dx.doi.org/10.1038/nclimate1629, 2012.

Durre, I. and Yin, X.: Enhanced radiosonde data for studies of vertical structure, Bulletin of the American Meteorological Society, 89, 1257–1261, https://doi.org/10.1175/2008BAMS2603.1, 2008.

Estep, M. F. and Hoering, T. C.: Biogeochemistry of the stable hydrogen isotopes, Geochimica et Cosmochimica Acta, 44, 1197–1206, https://doi.org/10.1016/0016-7037(80)90073-3, http://www.sciencedirect.com/science/article/pii/0016703780900733, 1980.

Fiorella, R. P., Poulsen, C. J., Zolá, R. S. P., Jeffery, M. L., and Ehlers, T. A.: Modern and long-term evaporation of central Andes surface waters suggests paleo archives underestimate Neogene elevations, Earth and Planetary Science Letters, 432, 59–72, https://doi.org/10.1016/j.epsl.2015.09.045, www.elsevier.com/locate/epsl, 2015.

Friedman, I. and O'Neil, J. R.: Data of geochemistry: Compilation of stable isotope fractionation factors of geochemical interest, vol. 440, US Government Printing Office, 1977.

Gat, J. R.: Oxygen and Hydrogen Isotopes in the Hydrologic Cycle, Annual Review of Earth and Planetary Sciences, 24, 225–262, https://doi.org/10.1146/annurev.earth.24.1.225, http://www.annualreviews.org/doi/10.1146/annurev.earth.24.1.225, 1996.

Gillies, R. R., Wang, S.-Y., Yoon, J.-H., and Weaver, S.: CFS Prediction of Winter Persistent Inversions in the Intermountain Region, Weather and Forecasting, 25, 1211–1218, https://doi.org/10.1175/2010WAF2222419.1, http://journals.ametsoc.org/doi/abs/10.1175/2010WAF2222419.1, 2010.

Gorski, G., Strong, C., Good, S. P., Bares, R., Ehleringer, J. R., and Bowen, G. J.: Vapor hydrogen and oxygen isotopes reflect water of combustion in the urban atmosphere., Proceedings of the National Academy of Sciences of the United States of America, 112, 3247–52, https://doi.org/10.1073/pnas.1424728112, http://www.pnas.org/content/112/11/3247.short, 2015.

Green, M. C., Chow, J. C., Watson, J. G., Dick, K., and Inouye, D.: Effects of snow cover and atmospheric stability on winter PM2.5 concentrations in western U.S. Valleys, Journal of Applied Meteorology and Climatology, 54, 1191–1201, https://doi.org/10.1175/JAMC-D-14-0191.1, 2015.

Horel, J., Splitt, M., Dunn, L., Pechmann, J., White, B., Ciliberti, C., Lazarus, S., Slemmer, J., Zaff, D., and Burks, J.: MesoWest: Cooperative mesonets in the western United States, Bulletin of the American Meteorological Society, 83, 211–225, https://doi.org/10.1175/1520-0477(2002)083<0211:MCMITW>2.3.CO;2, 2002.

Horita, J. and Wesolowski, D. J.: Liquid-vapor fractionation of oxygen and hydrogen isotopes of water from the freezing to the critical temperature, Geochimica et Cosmochimica Acta, 58, 3425–3437, https://doi.org/10.1016/0016-7037(94)90096-5, 1994.

Horváth, B., Hofmann, M., and Pack, A.: On the triple oxygen isotope composition of carbon dioxide from some combustion processes, Geochimica et Cosmochimica Acta, 95, 160–168, https://doi.org/10.1016/j.gca.2012.07.021, http://linkinghub.elsevier.com/retrieve/pii/S0016703712004139, 2012.

Keeling, C. D.: The concentration and isotopic abundances of atmospheric carbon dixoide in rural areas, Geochimica et Cosmochimica Acta, 13, 322–334, 1958.

Keeling, C. D.: The concentration and isotopic Abundances of Carbon Dioxide in rural and marine air, Geochimica et Cosmochimica Acta, 24, 277–298, 1961.

Lareau, N. P., Crosman, E., Whiteman, C. D., Horel, J. D., Hoch, S. W., Brown, W. O. J., and Horst, T. W.: The persistent cold-air pool study, Bulletin of the American Meteorological Society, 94, 51–63, https://doi.org/10.1175/BAMS-D-11-00255.1, 2013.

Majoube, M.: Fractionation factor of 18O between water vapour and ice, Nature, 226, 1242, 1970.

Malek, E., Davis, T., Martin, R. S., and Silva, P. J.: Meteorological and environmental aspects of one of the worst national air pollution episodes (January, 2004) in Logan, Cache Valley, Utah, USA, Atmospheric Research, 79, 108–122, https://doi.org/10.1016/j.atmosres.2005.05.003, 2006.

Merlivat, L. and Nief, G.: Isotopic fractionation of solid-vapor and liquid-vapor changes of state of water at temperatures below 0° C, Tellus, 19, 122–127, 1967.

Miller, J. B. and Tans, P. P.: Calculating isotopic fractionation from atmospheric measurements at various scales, Tellus, Series B: Chemical and Physical Meteorology, 55, 207–214, https://doi.org/10.1034/j.1600-0889.2003.00020.x, 2003.

Pataki, D. E., Bowling, D. R., Ehleringer, J. R., and Zobitz, J. M.: High resolution atmospheric monitoring of urban carbon dioxide sources, Geophysical Research Letters, 33, 1–5, https://doi.org/10.1029/2005GL024822, 2006.

Patarasuk, R., Gurney, K. R., O'Keeffe, D., Song, Y., Huang, J., Rao, P., Buchert, M., Lin, J. C., Mendoza, D., and Ehleringer, J. R.: Urban high-resolution fossil fuel CO2 emissions quantification and exploration of emission drivers for potential policy applications, Urban Ecosystems, 19, 1013–1039, https://doi.org/10.1007/s11252-016-0553-1, http://dx.doi.org/10.1007/s11252-016-0553-1, 2016.

Rozanski, K., Araguás-Araguás, L., and Gonfiantini, R.: Isotopic Patterns in Modern Global Precipitation, in: Climate Change in Continental Isotopic Records, edited by Swart, P. K., Lohmann, K. C., McKenzie, J., and Savin, S. M., pp. 1–36, American Geophysical Union, Washington, DC, 1993.

Sailor, D. J.: A review of methods for estimating anthropogenic heat and moisture emissions in the urban environment, International Journal of Climatology, 31, 189–199, https://doi.org/10.1002/joc.2106, 2011.

Salmon, O. E., Shepson, P. B., Ren, X., Marquardt Collow, A. B., Miller, M. A., Carlton, A. G., Cambaliza, M. O., Heimburger, A., Morgan, K. L., Fuentes, J. D., Stirm, B. H., Grundman, R., and Dickerson, R. R.: Urban emissions of water vapor in winter, Journal of Geophysical Research: Atmospheres, 122, 9467–9484, https://doi.org/10.1002/2016JD026074, 2017.

Seidel, D. J., Zhang, Y., Beljaars, A., Golaz, J.-C., Jacobson, A. R., and Medeiros, B.: Climatology of the planetary boundary layer over the continental United States and Europe, Journal of Geophysical Research: Atmospheres, 117, n/a–n/a, https://doi.org/10.1029/2012JD018143, http://doi.wiley.com/10.1029/2012JD018143, 2012.

Sessions, A. L., Burgoyne, T. W., Schimmelmann, A., and Hayes, J. M.: Fractionation of hydrogen isotopes in lipid biosynthesis, Organic Geochemistry, 30, 1193–1200, https://doi.org/10.1016/S0146-6380(99)00094-7, 1999.

Trenberth, K. E., Fasullo, J., Smith, L., Qian, T., and Dai, A.: Estimates of the Global Water Budget and Its Annual Cycle Using Observational and Model Data, Journal of hydrometeorology - special section, 8, 758–769, https://doi.org/10.1175/JHM600.1, 2006.

Vogelezang, D. H. P. and Holtslag, A. A. M.: Evaluation and model impacts of alternative boundary-layer height formulations, Boundary-Layer Meteorology, 81, 245–269, 1996.

Webster, C. R. and Heymsfield, A. J.: Water isotope ratios D/H, 18O/16O, 17O/16O in and out of clouds map dehydration pathways., Science, 302, 1742–1745, https://doi.org/10.1126/science.1089496, 2003.

Whiteman, C. D., Bian, X., and Zhong, S.: Wintertime evolution of the temperature inversion in the Colorado Plateau Basin, Journal of Applied Meteorology, 38, 1103–1117, https://doi.org/10.1175/1520-0450(1999)038<1103:WEOTTI>2.0.CO;2, 1999.

Whiteman, C. D., Zhong, S., Shaw, W. J., Hubbe, J. M., Bian, X., and Mittelstadt, J.: Cold Pools in the Columbia Basin, Weather and Forecasting, 16, 432–447, https://doi.org/10.1175/1520-0434(2001)016<0432:CPITCB>2.0.CO;2, 2001.

Whiteman, C. D., Hoch, S. W., Horel, J. D., and Charland, A.: Relationship between particulate air pollution and meteorological variables in Utah's Salt Lake Valley, Atmospheric Environment, 94, 742–753, https://doi.org/10.1016/j.atmosenv.2014.06.012, 2014.

Zhao, C. L. and Tans, P. P.: Estimating uncertainty of the WMO mole fraction scale for carbon dioxide in air, Journal of Geophysical Research Atmospheres, 111, 1–10, https://doi.org/10.1029/2005JD006003, 2006.